

Composite-fringe atom interferometry for high dynamic-range sensing

Chen Avinadav,^{1,2,*} Dmitry Yankelev,^{1,2,†} Ofer Firstenberg,¹ and Nir Davidson¹

¹*Department of Physics of Complex Systems, Weizmann Institute of Science, Rehovot 7610001, Israel*

²*Rafael Ltd, Haifa 3102102, Israel*

Atom interferometers offer excellent sensitivity to gravitational and inertial signals but have limited dynamic range. We introduce a scheme that improves on this trade-off by a factor of 50 using composite fringes, obtained from sets of measurements with slightly varying interrogation times. We analyze analytically the performance gain in this approach and the trade-offs it entails between sensitivity, dynamic range, and temporal bandwidth, and we experimentally validate the analysis over a wide range of parameters. By combining composite-fringe measurements with a particle-filter estimation protocol, we demonstrate continuous tracking of a rapidly varying signal over a span two orders of magnitude larger than the dynamic range of a traditional atom interferometer.

Cold atom interferometers [1] are highly sensitive and accurate sensors of gravitational [2–4] and inertial forces [5–10]. In addition to laboratory-based experiments in fundamental physics, such as tests of general relativity [11–15] and precision measurement of physical constants [16–20], atom interferometers for field-applications are being developed by several groups worldwide [21]. Mobile atomic gravimeters and gravity-gradiometers [22–31] have been demonstrated for geophysical surveys on land [22, 30], at sea [32], and in the air [33], while cold atom accelerometers and gyroscopes are developed for inertial navigation [34, 35]. Such field-based applications motivate the development of advanced techniques in atom interferometers to make them better suited for operating under conditions of large uncertainty and large temporal variations in the measured signal.

As a phase-measuring instrument, a trade-off exists between the sensitivity of an atom interferometer and its ambiguity-free dynamic range. The ratio of dynamic range to sensitivity is in general constant and depends only on the signal-to-noise ratio, whereas the scale factor, which determines their absolute values, may be controlled, *e.g.*, by changing the interferometer interrogation time T . When prior knowledge of the measured signal is insufficient, a standard approach involves initial measurements with low sensitivity and high dynamic range (*i.e.*, short T) and gradual progress to measurements with high sensitivity and low dynamic range (*i.e.*, long T) [30]. However, the time-averaged sensitivity per $\sqrt{\text{Hz}}$ of such a sequence is greatly reduced due to the measurements performed at low sensitivity. Alternatively, simultaneous measurements using two interrogation times was demonstrated in a dual-species atom interferometer [36] with an improved dynamic range of $\times 5$ at the cost of added experimental complexity. Another approach to remove ambiguities of atom interferometers relies on combining a classical sensor with large dynamic range [37, 38]. This solution is particularly relevant for scenarios where the measured signal varies continuously in time and substantially changes from shot to shot. However, imperfections such as non-linearity and intrinsic noise of the classical sensor, transfer function errors, misalignment, and non-

rigid platforms may limit the usefulness of this technique in harsh conditions [32], necessitating prolonged operation at short T to extend the dynamic range and track the changing signal at the expense of sensitivity.

In this work, we introduce a new approach to atom interferometry which dramatically increases its dynamic range with little to no penalty on sensitivity. We perform a set of measurements with slightly varying values of T , corresponding to slightly different scale factors of the interferometer. Together, these measurements constitute a *composite fringe*. Both the phase and the frequency of the composite fringe encode the measured inertial signal, providing a non-ambiguous dynamic range larger than measurements with a single value of T . The increase in dynamic range scales inversely with the span of scale factors and can reach orders of magnitude, limited only by the experimental signal-to-noise ratio. In addition to a static demonstration, we apply the scheme in conjunction with a particle-filter estimator to successfully track rapidly-varying signals, which change by more than 2π between consecutive measurements and span hundreds of radians altogether while maintaining high sensitivity.

We apply the composite fringe approach in an atom interferometer operating in a Mach-Zehnder geometry and measuring gravitational acceleration [39]. A freely-falling cold-atom ensemble interacts with pulses of counter-propagating laser beams which stimulate two-photon

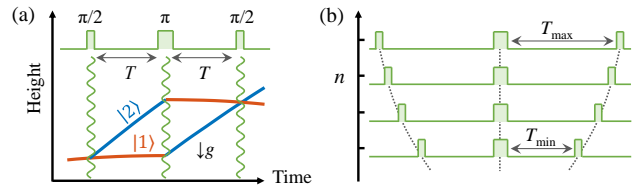


Figure 1. (a) Schematic diagram of an atomic gravimeter, operating in a $\pi/2$ - π - $\pi/2$ Mach-Zehnder geometry. Counter-propagating laser beams interact with the atoms and generate the interferometer sequence. (b) Composite-fringe atom interferometry comprises a set of measurements with interrogation times T that quadratically vary within a small range.

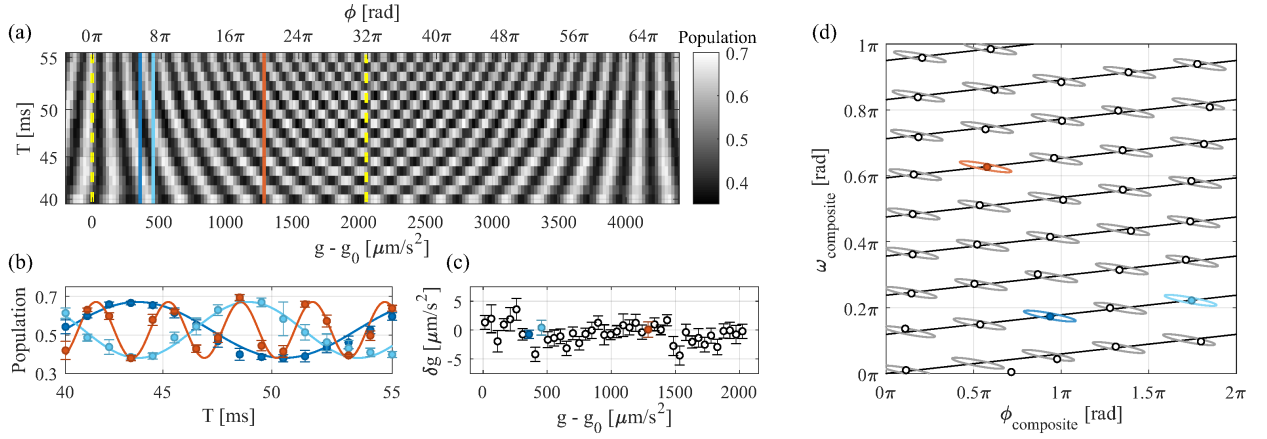


Figure 2. Composite-fringe atom interferometry. (a) Experimental data measured with $N = 16$ interrogation times between $T_{\min} = 40$ ms and $T_{\max} = 55$ ms. Different values of gravity are simulated by changing the chirp rate $\alpha = k_{\text{eff}}g_0$ of the Raman beams. Here, the ambiguity-free dynamic range (dashed lines) is extended by the composite-fringe approach to approximately 32π rad at T_{\max} , representing a 16-fold increase compared to a fringe measured at fixed T_{\max} . Data is averaged over 5 shots. (b) Composite fringes measured at different gravity values as indicated by colored lines in (a). Proximate gravity values (dark, bright blue) result in fringes with similar frequency but different phase, while a larger difference in gravity (red) renders a substantial change in frequency. Dots are measurements averaged over 5 shots, error bars are $\pm 1\sigma$, solid lines are sinusoidal fits. (c) Residual of the gravity value fitted from each composite fringe, over the span of one extended dynamic range. The resulting sensitivity is $1.7 \mu\text{m/s}^2$ per fringe, or $6.7 \mu\text{m/s}^2$ per shot, close to the $7.3 \mu\text{m/s}^2$ per shot obtained from standard fringes at fixed $T = T_{\max}$ in our apparatus. (d) Phase-frequency map of composite fringes: solid lines represent the theoretical prediction for gravity values within the first extended dynamic range; circles represent the phase and frequency extracted from fits to the fringe data in (a). Gravity increases from the bottom left corner to the top right. Ellipses represent the 95% confidence interval of the covariance matrix of phase and frequency estimation at the experimentally-characterized $\sigma_\phi = 400$ mrad.

transitions. A sequence of three pulses coherently splits, redirects, and recombines the atomic wave-packets in space [Fig. 1(a)]. The interferometer phase is given by $\phi = (k_{\text{eff}}g - \alpha)T^2 + \phi_L$, where k_{eff} is the effective atom optics two-photon wavevector, g is the gravitational acceleration, and T is the time between pulses. The relative frequency of the counter-propagating beams is chirped at a rate $\alpha = k_{\text{eff}}g_0$, where g_0 is an approximate value of the gravitational acceleration, in order to compensate the changing Doppler shift of the atoms during their free-fall. ϕ_L is a tunable laser phase applied during the final $\pi/2$ -pulse of the interferometer.

Our experimental apparatus is described in detail in Ref. [40]. Briefly, we trap and cool an ensemble of ^{87}Rb atoms and launch it on a free-fall trajectory using moving optical molasses. Vertical, retroreflected Raman beams, derived from a single laser diode using electro-optic modulation at 6.834 GHz, drive Doppler-sensitive two-photon transitions [41] between $|F = 1, m_F = 0\rangle$ and $|F = 2, m_F = 0\rangle$ for state initialization and interferometry sequence. The population fraction in $F = 2$, determined by state-dependent fluorescence, constitutes the interferometer output signal.

The standard fringe of an atom interferometer is $S(\phi) = A - (C/2)\cos\phi$, where A and C are the fringe offset and contrast. If this fringe is measured at N points (e.g., by scanning ϕ_L over 2π) using a single, fixed value of T , the gravitational phase $k_{\text{eff}}gT^2$ can be determined

with uncertainty σ_ϕ/\sqrt{N} . Here σ_ϕ is the total phase uncertainty *per shot* due to detection noise and phase noise [42]. This corresponds to a determination of gravity with uncertainty per shot of $\sigma_{g,\text{standard}} = \sigma_\phi / (k_{\text{eff}}T^2)$, over an ambiguity-free dynamic range of $\Delta g_{\text{standard}} = 2\pi / (k_{\text{eff}}T^2)$. The ratio of dynamic range to sensitivity-per-shot is therefore $(\Delta g/\sigma_g)_{\text{standard}} = 2\pi/\sigma_\phi$, which depends only on the measurement phase uncertainty.

Here instead, we form a composite fringe from a set of N measurements S_n , with the scale factor $k_{\text{eff}}T^2$ varying linearly with $n = 0, \dots, N - 1$, by choosing variable interrogation times [Fig. 1(b)],

$$T_n^2 = T_{\min}^2 + \frac{n}{N-1} (T_{\max}^2 - T_{\min}^2). \quad (1)$$

As shown in Figs. 2(a),(b), the series $\{S_n\}$ forms a new type of fringe, $S_n = A - (C/2)\cos(n\omega_{\text{comp}} + \phi_{\text{comp}})$, with

$$\phi_{\text{comp}} = (k_{\text{eff}}g - \alpha)T_{\min}^2 + \phi_L, \quad (2)$$

$$\omega_{\text{comp}} = (k_{\text{eff}}g - \alpha)\frac{T_{\max}^2 - T_{\min}^2}{N-1}. \quad (3)$$

Unlike the standard fringe with fixed T , here both phase and frequency depend on g , albeit with very different scale factors. While ϕ_{comp} varies rapidly with g and acts as a high-resolution measurement, similar to a standard measurement with fixed T , ω_{comp} varies slowly with g and acts as a coarse measurement, as exemplified in Fig. 2(d).

The composite-fringe frequency can be estimated unambiguously up to $\omega_{\text{comp}} = \pi$, resulting in the extended dynamic range $\Delta g_{\text{comp}} = \pi(N-1)/[k_{\text{eff}}(T_{\text{max}}^2 - T_{\text{min}}^2)]$. With respect to a fixed- T measurement sequence, we find an increase in dynamic range by a factor

$$\frac{\Delta g_{\text{comp}}}{\Delta g_{\text{standard}}} = \frac{1}{2} \frac{N-1}{1 - T_{\text{min}}^2/T_{\text{max}}^2}. \quad (4)$$

The sensitivity per shot of a composite fringe can be analytically derived [42] and is approximately

$$\sigma_{g,\text{comp}} \approx \frac{\sigma_{\phi}}{k_{\text{eff}}T_{\text{min}}T_{\text{max}}} = \frac{T_{\text{max}}}{T_{\text{min}}} \cdot \sigma_{g,\text{standard}}. \quad (5)$$

As T_{min} approaches T_{max} , the penalty in $\sigma_{g,\text{comp}}$ becomes negligible while the gain in dynamic range compared to a standard fringe measurement becomes dramatic. Indeed, Fig. 2(c) presents the residuals δg of the values of g as obtained by single-parameter fits to the measured composite fringes, exhibiting similar sensitivity to measurements at fixed $T = T_{\text{max}}$.

The potential gain in dynamic range is limited by σ_{ϕ} . Primarily, when the uncertainty in estimating the phase and frequency of the composite fringe is comparable to the distance between lines in Fig. 2(d), a *line jump* may occur and result in a large error in estimating g . The criterion for avoiding large errors is approximately [42]

$$\frac{\sqrt{N}(T_{\text{max}}^2 - T_{\text{min}}^2)}{\sigma_{\phi} T_{\text{min}}T_{\text{max}}} \gg 1. \quad (6)$$

Notably, the potential gain in dynamic range increases if σ_{ϕ} decreases, as T_{min} can approach T_{max} without increasing the probability of large estimation errors. Conversely, the error probability may be reduced by increasing N , which also serves to increase the dynamic range, at the cost of temporal bandwidth.

To understand the trade-offs in the composite fringe approach, we present in Fig. 3(a) the projected gain in dynamic range compared to operation in fixed- T and the corresponding probability of error. The error probability was evaluated for total phase uncertainty $\sigma_{\phi} = 400$ mrad. This value was experimentally characterized in our apparatus for interrogation times near 50 ms and is primarily due to vibrations. Operating at $N \lesssim 20$, corresponding to typical atom-interferometry temporal bandwidths, and requiring error probabilities below 10^{-2} , we can operate at $T_{\text{min}}/T_{\text{max}} \approx 0.85$ and gain more than an order of magnitude in dynamic range. For larger N , ratios $T_{\text{min}}/T_{\text{max}}$ of over 0.9 become possible, enabling gains of over two orders of magnitude.

To test the model predictions, we measured hundreds of composite fringes between $T_{\text{min}} = 40$ ms and $T_{\text{max}} = 55$ ms over $N = 49$ points at a constant chirp rate α , and analyzed the results in subsets of different N and T_{min} values. Measurements at fixed $T = 55$ ms were also

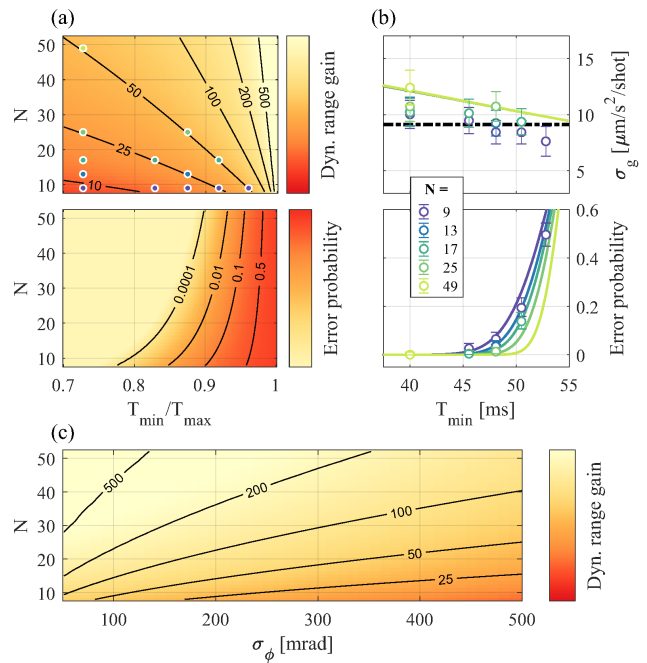


Figure 3. (a) Projected performance of composite fringes compared to standard measurement at fixed T . Top: Gain in dynamic range [Eq. 4]. Bottom: Error probability [Eq. A.10 in SI [42], evaluated with $\sigma_{\phi} = 400$ mrad]. (b) Experimental results: Sensitivity *per shot* (top) and error probability (bottom) as a function of T_{min} , with $T_{\text{max}} = 55$ ms, for different values of N as indicated in the legend. Measurements (circles) are averaged over 230 composite fringes, and error bars represent confidence interval of 68%. The results are in excellent agreement with the analytic predictions (solid lines). Dashed line represents a reference measurement with fixed $T = 55$ ms. Increase in dynamic range at the measured set points is indicated by filled circles in (a). (c) Projected gain in dynamic range as a function of σ_{ϕ} and N , for a threshold error probability of 10^{-2} .

performed for reference. Figure 3(b) shows that the composite fringes results are in excellent agreement with the analytical model with no fit parameters.

Figure 3(c) summarizes the gain in dynamic range for different values of phase uncertainty, at a fixed error probability threshold of 10^{-2} , a value where large errors may be removed with outlier detection with little sacrifice in sensitivity or bandwidth. A large and realistic parameter space exists where the dynamic range increases by more than $\times 100$ at high temporal bandwidth.

The analysis thus far assumes that the measured signal is static or slowly varying with respect to the time it takes to measure N points of a composite fringe, as in stationary gravity measurements. We now turn our focus to dynamic scenarios, such as mobile gravity surveys or inertial measurements onboard a navigating platform, where the measured signal may change by more than $\pm\pi$ from shot to shot and result in phase ambiguities. To address this challenge and track a dynamic signal, we

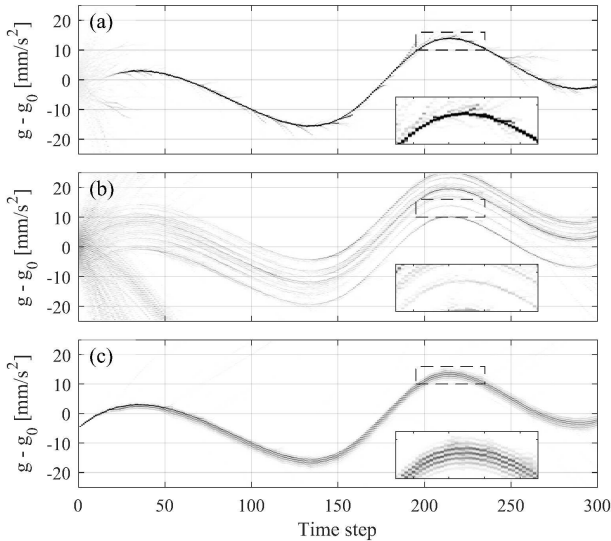


Figure 4. Time-dependent particle filter histograms in an experiment with large and rapid changes in g . (a) Composite-fringe atom interferometry ($N = 12$, $T_{\min} = 20$ ms, $T_{\max} = 30$ ms, corresponding to $\Delta g_{\text{comp}} = 4.3$ mm/s²). The filter is given the initial conditions $g = g_0$, $\dot{g} = 0$ with uncertainties $\sigma_g = 5$ mm/s², $\sigma_{\dot{g}} = 1.5$ mm/s²/shot. (b) Standard fixed- T measurements ($T = 30$ ms), initial conditions as in (a). Colormap is scaled to emphasize the multiple weak trajectories of particles. (c) Same as (b), with ideal initial conditions and zero initial uncertainty. Insets depict the single solution found by the filter using the composite-fringe approach (a) versus the ambiguity of standard fixed- T measurements (b,c).

combine the composite-fringe approach with an estimation protocol employing particle-filter methodology.

Particle filtering is a sequential Monte-Carlo estimation method based on the Bayesian principle [43, 44]. A large set of weighted particles is used to estimate the posterior distribution of unknown state-variables based on inaccurate observations or measurements. This approach is especially suited for problems with multimodal likelihood functions, such as ambiguous phase measurements, and where the resulting (posterior) state distribution is very different from Gaussian. Each time step of the filter consists of two main actions: First, particles propagate in state space according to an underlying system model, forming a prediction of the new state. Second, the particles are weighted according to their likelihood given the current observed measurements. Occasionally the particles are resampled with equal weights to avoid degeneracy where only a few particles have non-zero weights. Our implementation of the particle filter [42] tracks g and \dot{g} as the state variables, with random process noise added to the derivatives at each time step.

An experimental demonstration of the composite-fringe approach combined with particle filtering is shown in Fig. 4(a). By varying the Raman-lasers chirp rate α between subsequent shots, we simulate a random gravity

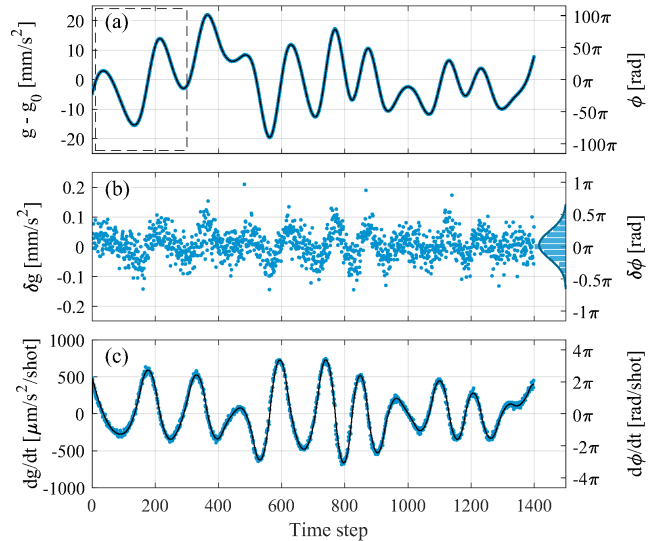


Figure 5. Experimental results of composite fringe and particle filtering with a dynamic signal. (a) Gravity estimation (blue) compared to the known input signal (black, barely discernible at this scale). Changes in g correspond to $\pm 100\pi$ rad at T_{\max} , a hundred-fold improvement in dynamic range. Dashed lines indicate the region shown in Fig. 4(a). (b) Residuals of the fitted signal, with $\sigma_g = 46$ $\mu\text{m/s}^2$ per shot (see histogram), compared to expected 15 $\mu\text{m/s}^2$ per shot at these experimental conditions. Excess noise is attributed to imperfection in the realization of the particle filter. (c) \dot{g} estimated by the filter (blue) compared to the input signal (black). Shot-to-shot changes of up to $\pm 3\pi$ rad/shot at T_{\max} are evident.

signal with high frequencies and large amplitude, which may arise, for example, in mobile gravimetry. T is varied over $N = 12$ values between $T_{\min} = 20$ and $T_{\max} = 30$ ms, for which $\sigma_\phi = 140$ mrad in our apparatus. To enhance the information gained by the filter at every time step, T is sampled as $T_1, T_{N/2+1}, T_2, T_{N/2+2}, \dots$ rather than sequentially. Following an initial uncertainty period, the particles quickly converge on the correct solution. New possible solutions periodically emerge but they are quickly dismissed by the filter due to incompatibility with incoming observations.

For comparison, Fig. 4(b) presents the same time-varying gravity signal measured with fixed T . In this case, many different trajectories remain likely as the filter is unable to converge on the correct solution due to large ambiguities. Finally, Fig. 4(c) shows the filter results with fixed T when the initial conditions of g and \dot{g} are assumed to be precisely known. Even in this ideal and impractical scenario, fixed- T measurements result in ambiguities emerging over time and the exact solution for g cannot be reliably determined.

Figure 5 presents a complete analysis of the measured data, using forward- and backward-propagating particles to avoid edge effects [42]. The filter tracks with high fidelity and high temporal resolution the varying signal,

which spans a dynamic range 100-times larger than a standard fringe at T_{\max} and which includes changes of more than $\pm 3\pi$ rad/shot. Further optimization of the filter and estimation protocol may improve the resulting short-term sensitivity compared to expected performance at T_{\max} and reduce the visible effects of under- and over-estimation of the signal at its local minima and maxima [Fig. 5(b)]. Additional improvement can be achieved by real-time estimation and prediction of g , which would allow tuning the interferometer approximately to mid-fringe at every measurement, and even more so by incorporating quadrature phase measurement [36, 40].

In conclusion, we introduce composite-fringe atom interferometry, employing measurement sets with variable interrogation times. This new approach provides orders-of-magnitude gain in dynamic range by overcoming the traditional trade-off between phase sensitivity and non-ambiguity in interferometric sensors. An analytical model for the sensitivity and error probability has been developed and compared to the experimental study with excellent agreement. When measuring static or slowly varying signals, composite fringes allow high-sensitivity operation in the presence of large initial uncertainty of the measured signal. For dynamic scenarios, we have demonstrated the integration of a particle-filter estimator for tracking dynamic signals which are impossible to measure with traditional interferometry schemes without compromising sensitivity.

The composite-fringe approach could prove valuable for field applications of atom interferometry, such as mobile gravity surveys or onboard navigation. While the discussion and experimental demonstration here focused on atomic gravimeters, this approach can be applied to other cold atom sensors, including gravity gradiometers and gyroscopes, as well as other interferometry-based quantum sensors such as magnetometers.

We thank Ran Fischer, Roy Shaham, and Tal David for valuable discussions. This work was supported by the Pazy Foundation and the Israel Science Foundation.

C.A and D.Y. contributed equally to this work.

* Electronic address: chen.avinadav@weizmann.ac.il

† Electronic address: dimitry.yankelev@weizmann.ac.il

- [1] G. M. Tino and M. A. Kasevich, eds., *Atom Interferometry, in Proceedings of the International School of Physics "Enrico Fermi," Course CLXXXVIII* (Societa Italiana di Fisica and IOS Press, 2014).
- [2] A. Peters, K. Y. Chung, and S. Chu, *Metrologia* **38**, 25 (2001).
- [3] M. Snadden, J. McGuirk, P. Bouyer, K. Haritos, and M. Kasevich, *Physical Review Letters* **81**, 971 (1998).
- [4] F. Sorrentino, A. Bertoldi, Q. Bodart, L. Cacciapuoti, M. de Angelis, Y.-H. Lien, M. Prevedelli, G. Rosi, and G. M. Tino, *Applied Physics Letters* **101**, 114106 (2012).
- [5] B. Barrett, R. Geiger, I. Dutta, M. Meunier, B. Canuel, A. Gauguet, P. Bouyer, and A. Landragin, *Comptes Rendus Physique* **15**, 875 (2014).
- [6] B. Canuel, F. Leduc, D. Holleville, A. Gauguet, J. Fils, A. Virdis, A. Clairon, N. Dimarcq, C. J. Bordé, A. Landragin, and P. Bouyer, *Physical Review Letters* **97** (2006), 10.1103/physrevlett.97.010402.
- [7] J. K. Stockton, K. Takase, and M. A. Kasevich, *Physical Review Letters* **107** (2011), 10.1103/physrevlett.107.133001.
- [8] T. L. Gustavson, P. Bouyer, and M. A. Kasevich, *Physical Review Letters* **78**, 2046 (1997).
- [9] D. Savoie, M. Altorio, B. Fang, L. A. Sidorenkov, R. Geiger, and A. Landragin, *Science Advances* **4**, eaau7948 (2018).
- [10] S. M. Dickerson, J. M. Hogan, A. Sugarbaker, D. M. S. Johnson, and M. A. Kasevich, *Physical Review Letters* **111** (2013), 10.1103/physrevlett.111.083001.
- [11] S. Dimopoulos, P. W. Graham, J. M. Hogan, and M. A. Kasevich, *Physical Review Letters* **98** (2007), 10.1103/physrevlett.98.111102.
- [12] H. Müller, A. Peters, and S. Chu, *Nature* **463**, 926 (2010).
- [13] M. A. Hohensee, S. Chu, A. Peters, and H. Müller, *Physical Review Letters* **106** (2011), 10.1103/physrevlett.106.151102.
- [14] D. N. Aguilera, H. Ahlers, B. Battelier, A. Bawamia, A. Bertoldi, R. Bondarescu, K. Bongs, P. Bouyer, C. Braxmaier, L. Cacciapuoti, C. Chaloner, M. Chwalla, W. Ertmer, M. Franz, N. Gaaloul, M. Gehler, D. Gerardi, L. Gesa, N. Gürlebeck, J. Hartwig, M. Hauth, O. Hellmig, W. Herr, S. Herrmann, A. Heske, A. Hinton, P. Ireland, P. Jetzer, U. Johann, M. Krutzik, A. Kubelka, C. Lammerzahl, A. Landragin, I. Lloro, D. Massonnet, I. Mateos, A. Milke, M. Nofriaris, M. Osswald, A. Peters, K. Posso-Trujillo, E. Rasel, E. Rocco, A. Roura, J. Rudolph, W. Schleich, C. Schubert, T. Schuldt, S. Seidel, K. Sengstock, C. F. Sopaerta, F. Sorrentino, D. Summers, G. M. Tino, C. Trenkel, N. Uzunoglu, W. von Klitzing, R. Walser, T. Wendrich, A. Wenzlawski, P. Wessels, A. Wicht, E. Wille, M. Williams, P. Windpassinger, and N. Zahzam, *Classical and Quantum Gravity* **31**, 115010 (2014).
- [15] L. Zhou, S. Long, B. Tang, X. Chen, F. Gao, W. Peng, W. Duan, J. Zhong, Z. Xiong, J. Wang, Y. Zhang, and M. Zhan, *Physical Review Letters* **115** (2015), 10.1103/physrevlett.115.013004.
- [16] D. S. Weiss, B. C. Young, and S. Chu, *Physical Review Letters* **70**, 2706 (1993).
- [17] J. B. Fixler, G. T. Foster, J. M. McGuirk, and M. A. Kasevich, *Science* **315**, 74 (2007).
- [18] R. Bouchendira, P. Cladé, S. Guellati-Khélifa, F. Nez, and F. Biraben, *Physical Review Letters* **106** (2011), 10.1103/physrevlett.106.080801.
- [19] G. Rosi, F. Sorrentino, L. Cacciapuoti, M. Prevedelli, and G. M. Tino, *Nature* **510**, 518 (2014).
- [20] R. H. Parker, C. Yu, W. Zhong, B. Estey, and H. Müller, *Science* **360**, 191 (2018).
- [21] K. Bongs, M. Holynski, J. Vovrosh, P. Bouyer, G. Condon, E. Rasel, C. Schubert, W. P. Schleich, and A. Roura, *Nature Reviews Physics* **1**, 731 (2019).
- [22] X. Wu, *Gravity Gradient Survey with a Mobile Atom Interferometer*, Ph.D. thesis, Stanford (2009).
- [23] Y. Bidel, O. Carraz, R. Charrière, M. Cadoret, N. Zahzam, and A. Bresson, *Applied Physics Letters* **102**, 144107 (2013).

- [24] T. Farah, C. Guerlin, A. Landragin, P. Bouyer, S. Gaffet, F. P. D. Santos, and S. Merlet, *Gyroscope and Navigation* **5**, 266 (2014).
- [25] C. Freier, M. Hauth, V. Schkolnik, B. Leykauf, M. Schilling, H. Wziontek, H.-G. Scherneck, J. Müller, and A. Peters, *Journal of Physics: Conference Series* **723**, 012050 (2016).
- [26] B. Barrett, L. Antoni-Micollier, L. Chichet, B. Battelier, T. Lévêque, A. Landragin, and P. Bouyer, *Nature Communications* **7** (2016), 10.1038/ncomms13786.
- [27] V. Ménoiret, P. Vermeulen, N. Le Moigne, S. Bonvalot, P. Bouyer, A. Landragin, and B. Desruelle, *Scientific Reports* **8**, 12300 (2018).
- [28] L. Zhu, *A cold atoms gravimeter for use in absolute gravity comparisons*, Ph.D. thesis, University of Birmingham (2018).
- [29] D. Becker, M. D. Lachmann, S. T. Seidel, H. Ahlers, A. N. Dinkelaker, J. Grosse, O. Hellmig, H. Müntinga, V. Schkolnik, T. Wendrich, A. Wenzlawski, B. Weps, R. Corgier, T. Franz, N. Gaaloul, W. Herr, D. Lüdtke, M. Popp, S. Amri, H. Duncker, M. Erbe, A. Kohfeldt, A. Kubelka-Lange, C. Braxmaier, E. Charron, W. Ertmer, M. Krutzik, C. Lämmerzahl, A. Peters, W. P. Schleich, K. Sengstock, R. Walser, A. Wicht, P. Windpassinger, and E. M. Rasel, *Nature* **562**, 391 (2018).
- [30] X. Wu, Z. Pagel, B. S. Malek, T. H. Nguyen, F. Zi, D. S. Scheirer, and H. Müller, *Science Advances* **5**, eaax0800 (2019).
- [31] A. Lamb, *A Cold Atom Gravity Gradiometer for Field Applications*, Ph.D. thesis, University of Birmingham (2019).
- [32] Y. Bidet, N. Zahzam, C. Blanchard, A. Bonnin, M. Cadoret, A. Bresson, D. Rouxel, and M. F. Lequentrec-Lalancette, *Nature Communications* **9** (2018), 10.1038/s41467-018-03040-2.
- [33] Y. Bidet, N. Zahzam, A. Bresson, C. Blanchard, M. Cadoret, A. V. Olesen, and R. Forsberg, <http://arxiv.org/abs/1910.06666v1>.
- [34] P. Cheiney, L. Fouché, S. Templier, F. Napolitano, B. Battelier, P. Bouyer, and B. Barrett, *Physical Review Applied* **10** (2018), 10.1103/physrevapplied.10.034030.
- [35] Y.-J. Chen, A. Hansen, G. W. Hoth, E. Ivanov, B. Pelle, J. Kitching, and E. A. Donley, *Physical Review Applied* **12** (2019), 10.1103/physrevapplied.12.014019.
- [36] A. Bonnin, C. Diboune, N. Zahzam, Y. Bidet, M. Cadoret, and A. Bresson, *Applied Physics B* **124** (2018), 10.1007/s00340-018-7051-5.
- [37] S. Merlet, J. L. Gouët, Q. Bodart, A. Clairon, A. Landragin, F. P. D. Santos, and P. Rouchon, *Metrologia* **46**, 87 (2009).
- [38] J. Lautier, L. Volodimer, T. Hardin, S. Merlet, M. Lours, F. P. D. Santos, and A. Landragin, *Applied Physics Letters* **105**, 144102 (2014).
- [39] M. Kasevich and S. Chu, *Physical Review Letters* **67**, 181 (1991).
- [40] D. Yankelev, C. Avinadav, N. Davidson, and O. Firstenberg, *Physical Review A* **100** (2019), 10.1103/physreva.100.023617.
- [41] M. Kasevich, D. S. Weiss, E. Riis, K. Moler, S. Kasapi, and S. Chu, *Physical Review Letters* **66**, 2297 (1991).
- [42] See supplementary information.
- [43] P. Del Moral, *Markov Processes and Related Fields* **2**, 555 (1996).
- [44] R. Van Der Merwe, A. Doucet, N. De Freitas, and E. A. Wan, in *Advances in neural information processing systems* (2001) pp. 584–590.

SUPPLEMENTARY INFORMATION

Appendix A: Analytical model of composite fringe atom interferometry

In this Appendix, we derive analytic expressions for the sensitivity and error probability of atomic interferometry with composite fringes. We begin with a composite fringe consisting of N variable- T measurements,

$$S_n = A - \frac{C}{2} \cos [n\omega(g) + \phi(g) + \delta\phi_n] + \delta S_n, \quad (\text{A.1})$$

with $n = 0, 1, \dots, N-1$. The contrast C and offset A are assumed to be known, and

$$\phi(g) = (k_{\text{eff}}g - \alpha) T_{\text{min}}^2 \quad \text{and} \quad \omega(g) = (k_{\text{eff}}g - \alpha) \frac{T_{\text{max}}^2 - T_{\text{min}}^2}{N-1} \quad (\text{A.2})$$

are the unknown effective phase and frequency, as given in Eqs. (2)-(3) of the main text. The fringe function explicitly includes the random variables δS_n and $\delta\phi_n$, representing realizations of detection noise and phase noise, respectively, with variances σ_{det}^2 and σ_{phase}^2 . The most dominant contribution is usually phase noise due to mechanical vibrations of the mirror retroreflecting the Raman beams, whose position sets the frame of reference in which the atomic motion is measured. For small phase noise, it is convenient to approximate the two noise terms by a single effective detection noise $\delta\bar{S}_n$,

$$S_n \approx A - \frac{C}{2} \cos [n\omega(g) + \phi(g)] + \delta\bar{S}_n, \quad (\text{A.3})$$

whose variance is given by

$$\bar{\sigma}^2 = \left(\frac{1}{\sigma_{\text{det}}^2} + \frac{8}{C^2 \sigma_{\text{phase}}^2} \right)^{-1}. \quad (\text{A.4})$$

The total phase uncertainty per shot, as defined in the main text, is given by $\sigma_\phi = 2\sqrt{2}\bar{\sigma}/C$. In the limit of pure phase noise we have, as expected, $\sigma_\phi = \sigma_{\text{phase}}$.

(1) Sensitivity

We examine the estimator $\boldsymbol{\theta} = [\phi, \omega]^T$ of the unknown parameters $[\phi(g), \omega(g)]^T$, and we are interested in the uncertainty of $\boldsymbol{\theta}$, as given by its covariance $\text{cov}(\boldsymbol{\theta})$. To this end, we adopt the framework of maximum likelihood estimation. Given the set of measurements S_n , the likelihood function of $\boldsymbol{\theta}$ is given by

$$p(S_n; \boldsymbol{\theta}) = \frac{1}{(2\pi\bar{\sigma}^2)^{N/2}} \exp \left[-\frac{1}{2\bar{\sigma}^2} \sum_{n=0}^{N-1} (S_n - S(n, \boldsymbol{\theta}))^2 \right], \quad (\text{A.5})$$

with $S(n, \boldsymbol{\theta}) = A - (C/2) \cos(n\omega + \phi)$. The Fisher information matrix is

$$[I(\boldsymbol{\theta})]_{i,j} = -E \left[\frac{\partial^2 \ln p(S_n; \boldsymbol{\theta})}{\partial \theta_i \partial \theta_j} \right], \quad (\text{A.6})$$

where $E[\dots]$ denotes expectation value. Substituting Eq. (A.5) into Eq. (A.6), we find

$$I(\boldsymbol{\theta}) = \left(\frac{C}{2\bar{\sigma}} \right)^2 \frac{N(N-1)}{12} \begin{pmatrix} 6/(N-1) & 3 \\ 3 & (2N-1) \end{pmatrix}, \quad (\text{A.7})$$

where we assumed large N and that ω is not near 0 or π (the latter can be relaxed by deliberately varying ϕ_L when measuring a composite fringe). For an unbiased estimator of $\boldsymbol{\theta}$, the Cramér-Rao lower bound (CRLB) of the covariance matrix is given by $\text{cov}(\boldsymbol{\theta}) \geq I(\boldsymbol{\theta})^{-1}$, so

$$\text{cov}(\boldsymbol{\theta}) \geq \left(\frac{\bar{\sigma}}{C} \right)^2 \frac{16}{N(N+1)} \begin{pmatrix} 2(N-1) & -3 \\ -3 & 6/(N-1) \end{pmatrix}. \quad (\text{A.8})$$

Given the best estimated phase and frequency $\tilde{\theta}$, we now search for an estimator $\tilde{g} = \tilde{g}(\tilde{\theta})$ for the actual acceleration g . The optimal estimator is the value of \tilde{g} that minimizes the product $[\boldsymbol{\theta}(\tilde{g}) - \tilde{\theta}]^T I(\boldsymbol{\theta}) [\boldsymbol{\theta}(\tilde{g}) - \tilde{\theta}]$, where $\boldsymbol{\theta}(\tilde{g}) = [\phi(\tilde{g}), \omega(\tilde{g})]^T$, with $\phi(\tilde{g})$ and $\omega(\tilde{g})$ given in Eqs. (A.2). Performing the minimization for different values of $\tilde{\theta}$ yields the function $\tilde{g} = \tilde{g}(\tilde{\theta})$. With this function in hand, the uncertainty in estimating g is found by the transformation

$$\sigma_g^2 \geq \left[\frac{\partial \tilde{g}(\tilde{\theta})}{\partial \tilde{\theta}} \right]^T \text{cov}(\boldsymbol{\theta}) \left[\frac{\partial \tilde{g}(\tilde{\theta})}{\partial \tilde{\theta}} \right]. \quad (\text{A.9})$$

Using Eq. (A.8), we find

$$\sigma_g \geq \frac{\sqrt{8}\bar{\sigma}}{C k_{\text{eff}} T_{\text{max}} T_{\text{min}}} \left[1 + \frac{1}{6} \frac{2N-1}{N-1} \left(\frac{T_{\text{min}}}{T_{\text{max}}} \frac{T_{\text{max}}^2 - T_{\text{min}}^2}{T_{\text{min}}^2} \right)^2 \right]^{-1/2}, \quad (\text{A.10})$$

which, to leading order in $(T_{\text{max}}^2 - T_{\text{min}}^2)/T_{\text{min}}^2$ and in terms of the total phase uncertainty $\sigma_\phi = 2\sqrt{2}\bar{\sigma}/C$, simplifies to

$$\sigma_g \gtrsim \frac{\sigma_\phi}{k_{\text{eff}} T_{\text{max}} T_{\text{min}}}, \quad (\text{A.11})$$

as given in the main text.

(2) Large estimation error

We now turn to calculate the probability of a large estimation error, which results from a *jump* between the lines in the phase map [Fig. 2(d)]. First, we derive the uncertainty of the estimated phase and frequency along an axis perpendicular to these lines. The coordinate along this axis is defined as $p = -\phi \sin \alpha + \omega \cos \alpha$, with $\tan \alpha = (T_{\text{max}}^2 - T_{\text{min}}^2) / [T_{\text{min}}^2 (N-1)]$. The uncertainty in p is then given by a transformation similar to that in Eq. (A.9) and found to be

$$\sigma_p = 4 \frac{C}{\bar{\sigma}} \sqrt{\frac{6(N-1) T_{\text{min}}^2 T_{\text{max}}^2 + (2N-1)(T_{\text{max}}^2 - T_{\text{min}}^2)^2}{N(N+1)[(N-1)^2 T_{\text{min}}^4 + (T_{\text{max}}^2 - T_{\text{min}}^2)^2]}}, \quad (\text{A.12})$$

or, to leading order in $(T_{\text{max}}^2 - T_{\text{min}}^2)/T_{\text{min}}^2$,

$$\sigma_p \approx \frac{C}{\bar{\sigma}} \frac{T_{\text{max}}}{T_{\text{min}}} \sqrt{\frac{96}{N(N^2-1)}}. \quad (\text{A.13})$$

On the other hand, the distance between the lines is given by

$$\Delta p = \frac{2\pi (T_{\text{max}}^2 - T_{\text{min}}^2)}{\sqrt{(N-1)^2 T_{\text{min}}^4 + (T_{\text{max}}^2 - T_{\text{min}}^2)^2}}. \quad (\text{A.14})$$

From this we find the ratio, again to leading order in $(T_{\text{max}}^2 - T_{\text{min}}^2)/T_{\text{min}}^2$ and in terms of the total phase uncertainty σ_ϕ ,

$$\frac{\Delta p}{2\sigma_p} = \frac{\pi}{\sqrt{12}} \frac{1}{\sigma_\phi} \frac{(T_{\text{max}}^2 - T_{\text{min}}^2)}{T_{\text{min}} T_{\text{max}}} \sqrt{N \frac{N+1}{N-1}}. \quad (\text{A.15})$$

The probability of a large estimation error in g is then

$$\epsilon = 2 \left[1 - \Phi \left(\frac{\Delta p}{2\sigma_p} \right) \right], \quad (\text{A.16})$$

where $\Phi(x)$ is the normal cumulative distribution function.

Appendix B: Particle-filter implementation

In our implementation of the particle filter, we use the state variables g and \dot{g} to describe the dynamic system. The state of the m th particle at the i th time step is thus defined as

$$\mathbf{x}_{m,i} = \begin{bmatrix} g_{m,i} \\ \dot{g}_{m,i} \end{bmatrix}. \quad (\text{B.1})$$

The propagation model is given by $\mathbf{x}_{m,i+1} = \mathbf{F} \cdot \mathbf{x}_{m,i} + \mathbf{w}_{m,i}$, where the state propagation matrix \mathbf{F} is

$$\mathbf{F} = \begin{bmatrix} 1 & dt \\ 0 & 1 \end{bmatrix}, \quad (\text{B.2})$$

and $\mathbf{w}_{m,i}$ is a random process noise, distributed normally with zero mean and with a covariance given by

$$\mathbf{Q} = dt^2 \begin{bmatrix} 0 & 0 \\ 0 & \sigma_{\dot{g}}^2 \end{bmatrix}, \quad (\text{B.3})$$

where dt is the time increment between two measurements.

The input to the filter is the interferometer signal S_i , measured at each time step with a different interrogation time T_i . The filter also receives as input the interferometer fringe parameters A_i , C_i , which are found separately by collecting all measurements of the same interrogation time T_i and fitting their distribution. At each time step and for each particle, the residual is calculated as

$$r_{m,i} = S_i - \left[A_i - \frac{C_i}{2} \cos(k_{\text{eff}} g_{m,i} T_i^2) \right], \quad (\text{B.4})$$

from which the likelihood $p(\mathbf{x}_{m,i}|S_i)$ is determined based on the measurement noise model,

$$p(\mathbf{x}_{m,i}|S_i) = \frac{1}{\sqrt{2\pi\sigma^2}} \exp\left[-\frac{r_{m,i}^2}{2\sigma^2}\right]. \quad (\text{B.5})$$

Each particle is weighted according to its likelihood, and all particles are finally resampled at every time step with systematic resampling.

We used 5000 particles in the examples presented in the main text. Traditionally, at the end of each time step, the state variables are estimated as a weighted mean of all particles. We achieve more stable results by running the filter both forward and backward in time, calculating the time-dependent histogram of particles from both directions together, and running a ridge-detection algorithm (MATLAB `tfridge` function) on the combined histogram to find a continuous estimation of \tilde{g}_i . This analysis is less sensitive to temporary branching of the particles distribution.

A distribution of residuals of the measurement data can be calculated with respect to the estimated measurements, *i.e.*,

$$\tilde{r}_i = S_i - \left[A_i - \frac{C_i}{2} \cos(k_{\text{eff}} \tilde{g}_i T_i^2) \right]. \quad (\text{B.6})$$

The parameter $\sigma_{\tilde{g}}$ is determined by minimizing the variance of the \tilde{r}_i .